Supporting Information for

Ferroelastic nanodomain mediated mechanical switching of ferroelectricity in thick epitaxial films

Qian Li,[1,2,#,*] Bo Wang,[3,#] Qian He,[4] Pu Yu,[5] Long-Qing Chen,[3] Sergei V. Kalinin[2,*] and Jing-Feng Li[1,*]

1. State Key Laboratory of New Ceramics and Fine Processing, School of Materials Science and Engineering, Tsinghua University, Beijing 100084, China
2. Center for Nanophase Materials Science, Oak Ridge National Laboratory, TN 37831, USA
3. Department of Materials Science and Engineering, Pennsylvania State University, University Park, Pennsylvania 16802, USA
4. Department of Materials Science and Engineering, National University of Singapore, Singapore 119077
5. State Key Laboratory of Low Dimensional Quantum Physics and Department of Physics, Tsinghua University, Beijing 100084, China.

■ METHODS

Sample growth: ~100 nm $Pb(Zr_{0.2}Ti_{0.8})O_3$ thin films were epitaxially grown on (001)-$SrTiO_3$ single crystal substrates, using a reflection high-energy electron diffraction assisted pulsed laser deposition (RHEED-PLD) system with a 248 nm KrF excimer laser. A $SrRuO_3$ (SRO) buffer layer with thickness ~50 nm was first deposited, which serves as a bottom electrode. For the growth of the SRO layer, the substrate temperature was kept at 700 °C under an oxygen partial pressure of 100 mTorr and 90 mJ laser energy was used at a repetition rate of 16 Hz, while the corresponding parameters of 630 °C, 100 mTorr and 95 mJ at 3 Hz were used to deposit the PZT layer.

Synchrotron XRD: X-ray diffraction imaging was performed using the nanodiffraction instrument at the 7-ID-C beamline, Advanced Photon Source, Argonne National Laboratory. An 11 keV primary X-ray beam was focused to ~0.3 × 1 μm^2 size via a Fresnel zone plate and then brought onto the sample surface at incidence angles of 15–17°, resulting in a beam footprint of ~1 × 1 μm^2 (which defined the

lateral imaging resolution). This angular range traversed the specular reflection conditions for the PZT 002 Bragg peak. During imaging, the *xy*-positions of the sample were scanned at a fixed incidence angle, and diffracted X-rays were captured for each scan location using a Pilatus 100 K single photon-counting area detector placed ~0.5 m away from the sample. The sum intensities of several predefined regions of interest (ROI's) on the detector form images with different diffraction contrast.

STEM: Cross-sectional specimens of the PZT films for STEM analysis were prepared by the conventional procedures of mechanical thinning, precision polishing and ion milling down to electron transparency. High-angle annular dark-field (HAADF, Z-contrast) STEM images were taken using a Nion UltraSTEM operating at 200 kV, equipped with a cold field-emission electron gun and a corrector of third- and fifth-order aberrations. EELS mapping was taken using a Gatan Enfinium dual EELS system. Image analysis was performed via DigitalMicrograph software and ImageJ scripts.

PFM: Piezoresponse force microscopy was carried out in ambient environment using a commercial atomic force microscope (Asylum Research, Cypher AFM). Several makes of conductive AFM probes were used under a range of measurement conditions, including Nanosensor PPP-EFM (Si tip with Pt/Ir coating; stiffness: 2–5 N m^{-1}), ASYELEC-02 (Si tip with Pt/Ir coating; 20–30 N m^{-1}) and CDT-FMR (doped-diamond tip; 5–10 N m^{-1}); note that the diamond tips have a much larger nominal radius (83 nm vs 30 nm) than the metal-coated Si tips. The actual cantilever stiffness of the probes used was calibrated using the thermal noise method. PFM images were acquired typically using 0.5 V ac signals near contact resonance frequencies in the DART (dual ac resonance tracking) mode. For standard domain imaging, the scan speeds and contact setpoint were 1–20 μm s^{-1} and ~300 nN, respectively. To induce mechanical switching, loading forces up to several μN were applied while the tip was grounded (or otherwise stated). For the analysis of sequential PFM images as presented in Figure 3, OpenCV and Scikit-image libraries were employed to find and analyze domain wall contours within Python 2.7 software environment.

Phase-field simulation:

The phase-field simulation was performed by using the ferroelectric module of the μ-pro phase-field package (http://www.mupro.co/) which implements the semi-implicit Fourier transformation algorithm to iteratively solve the kinetic time-dependent Ginzburg-Laudau equation of a ferroelectric:

$$\frac{\partial \boldsymbol{P}}{\partial t} = -L\frac{\delta F}{\delta \boldsymbol{P}}$$

where the total free energy F consists of bulk, elastic, electric, and gradient contributions $F = \int (f_{bulk} + f_{elastic} + f_{electric} + f_{gradient}) dV$. At each time step, the elastostatic and electrostatic equations were solved self-consistently to obtain the driving forces of the polarization. Detailed expressions for each of the energy terms have been described in previous works and the corresponding parameters for $Pb(Zr_{0.2}Ti_{0.8})O_3$ were taken from Ref [40] . The scanning tip was modeled by assuming a surface traction distribution in the framework of Hertzian contact mechanics of a spherical indenter onto a half-space. The tip radius R was chosen as 30 nm while the Young's modulus E_{tip} and Poisson ratio ν_{tip} of a Pt tip were taken as $E_{tip} =$ 168 GPa and $\nu_{tip} =$ 0.30. Tip loading forces of up to 8 μN were applied.

■ SUPPLEMENTARY FIGURES

S1 Additional STEM results of 100 nm $Pb(Zr_{0.2}Ti_{0.8})O_3$ thin films

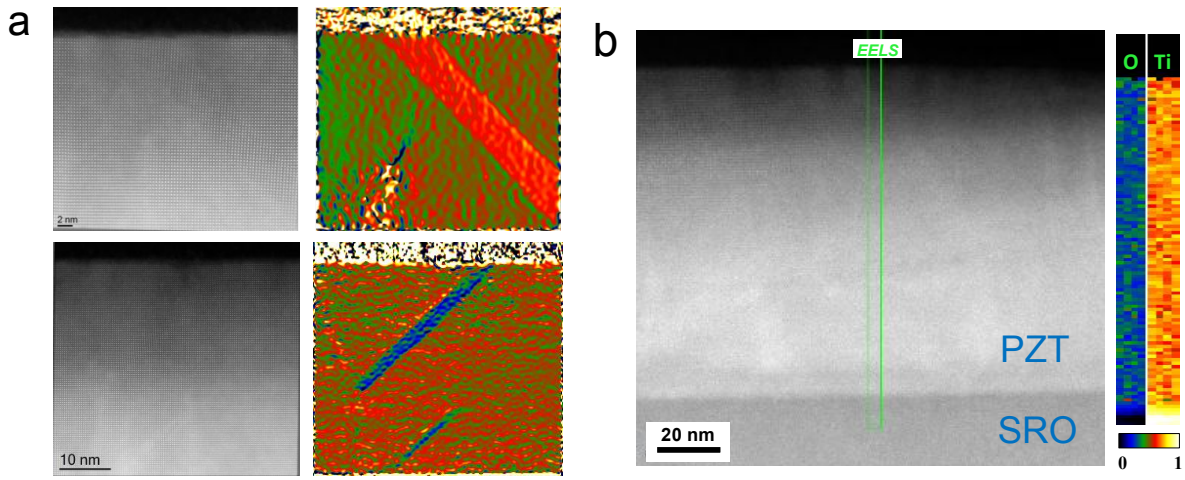

Figure S1 (a) HAADF images and corresponding GPA strain maps for other regions in the specimens. (b) Ti and O composition maps across the entire film thickness derived from quantitative EELS measurements.

S2 Comparison with electric switching

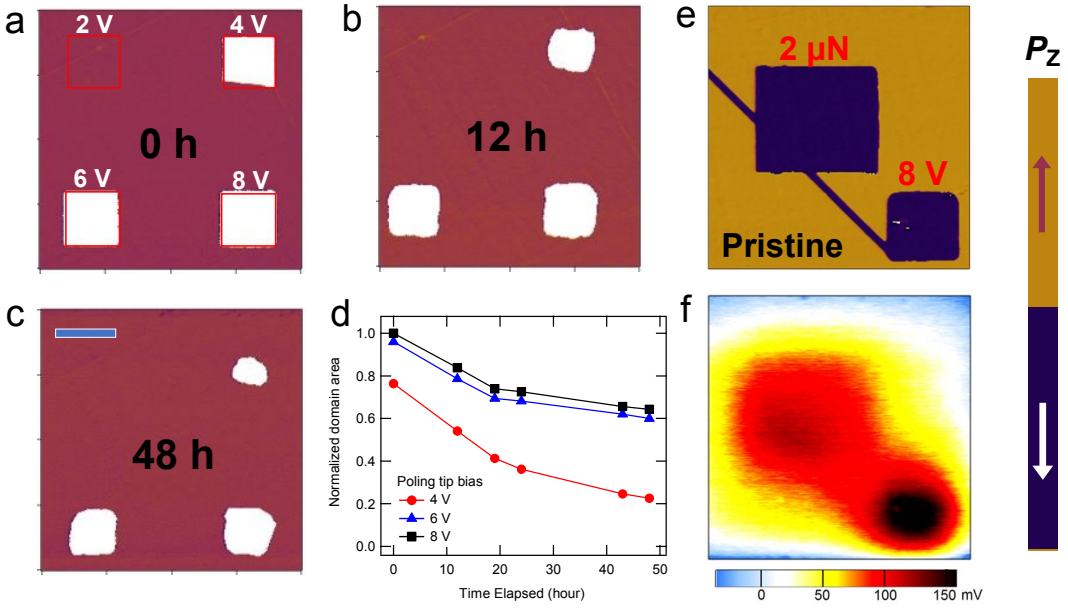

Figure S2 (a-c) PFM phase images of tip bias-written domains measured 0 h, 12 h and 48 h after the writing and (d) is a plot of the time evolution of the domain areas. (e) PFM images of two domains

written with tip bias and pressure and (f) corresponding surface potential images measured using Kelvin probe force microscopy (KPFM).

S3 Inhomogeneous pressure-induced switching behavior

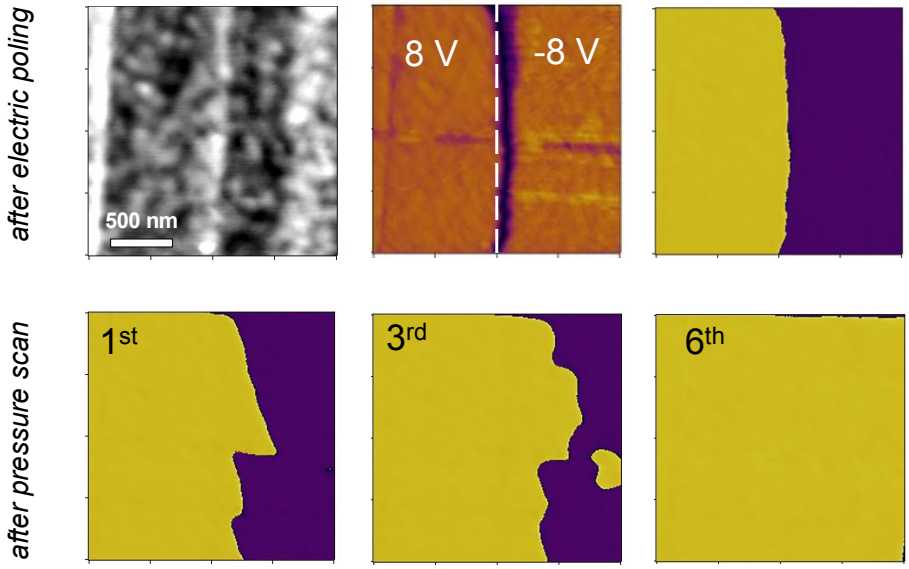

Figure S3 (a-c) Surface morphology, PFM amplitude and phase images of two domains written with a tip bias of +/- 8V; and (d-f) PFM phase images of the same region after mechanically scanned (tip-grounded) for one, three and six times.

S4 Control experiment of continuous PFM imaging

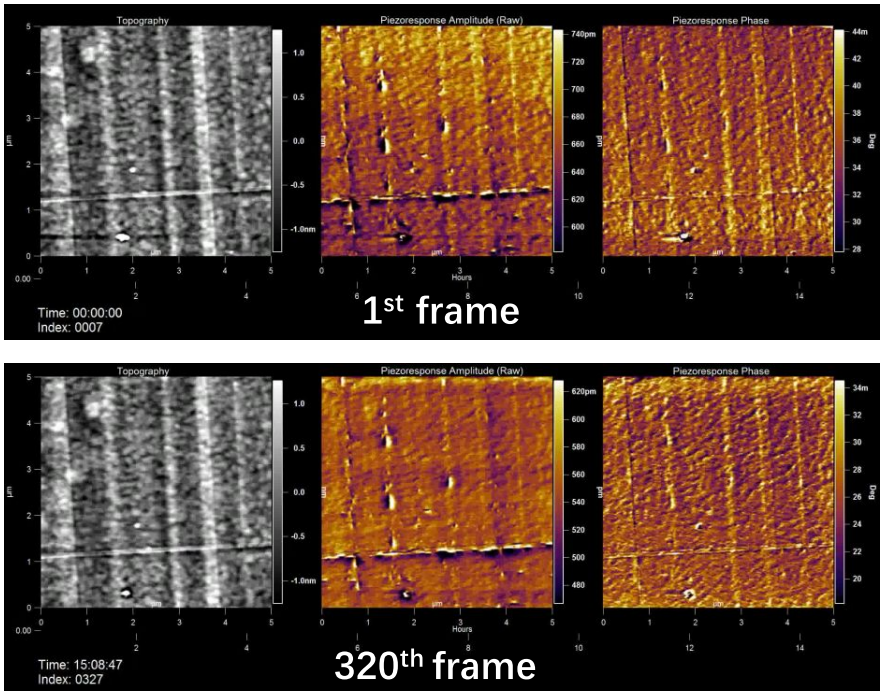

Figure S4 The upper row is the first PFM scan frame and the lower row is the 320th scan frame during continuous PFM imaging over the 5 × 5 μm^2 region using a loading force of 250 nN.

S5 Additional analysis for the incomplete switching dataset

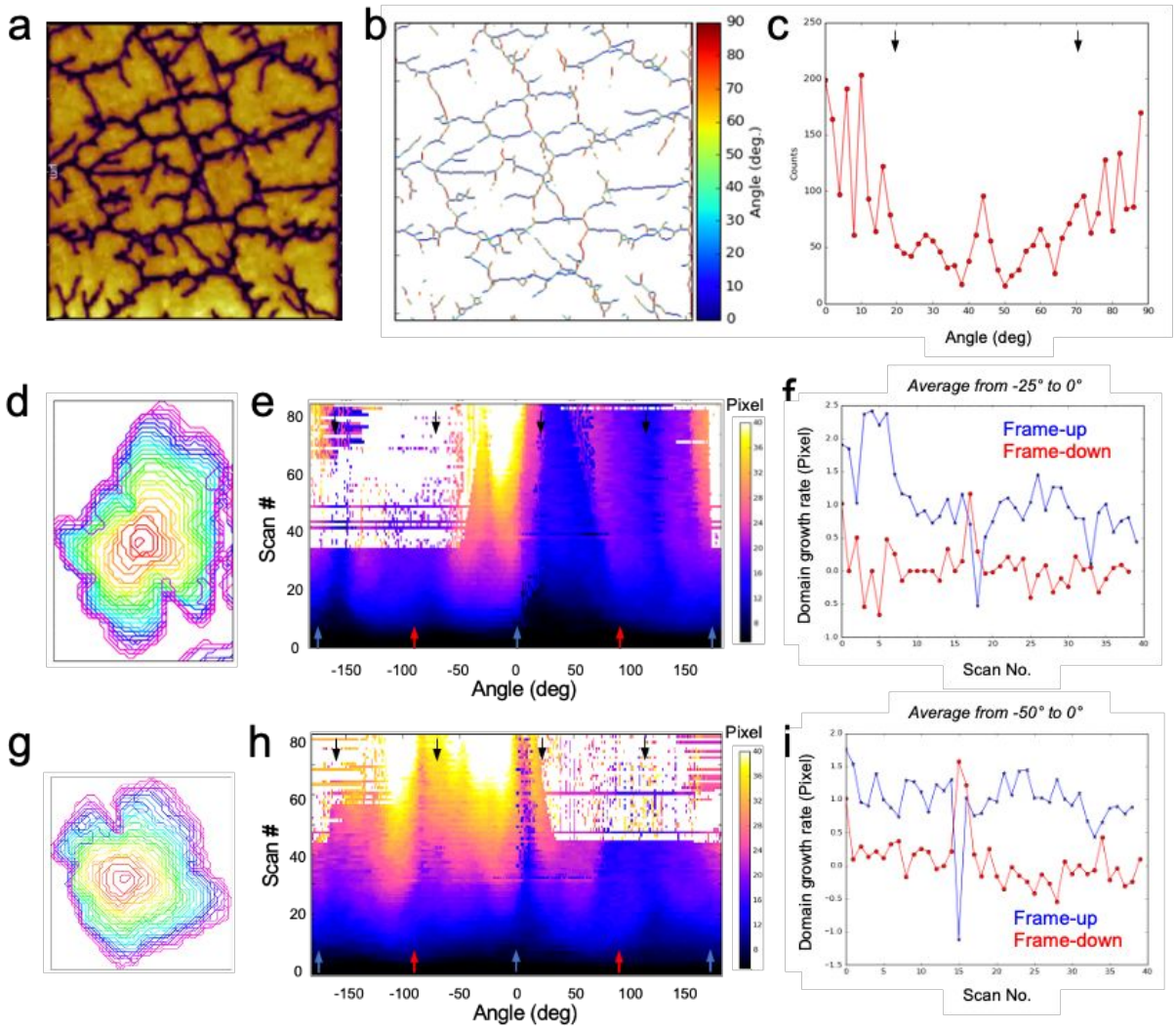

Figure S5 (a-c) Statistic analysis of the domain boundary orientations: (a) PFM amplitude image of the 340th scan, (b) extracted domain boundaries with the color scale representing the orientation angle and (c) histogram of the orientation angles. The arrows in (c) denote the directions of the ridge defects of the PZT thin films. (d-i) Domain growth rata analysis for another tow nucleation centers: (d,g) Overlay of domain boundary contours from the first 125 PFM images, (e,h) angle-resolved evolution of the domain boundary contours and (f,i) comparison between the frame-up and frame-down scans.

S6 Comparison between the (un)pinned ferroelastic domain models

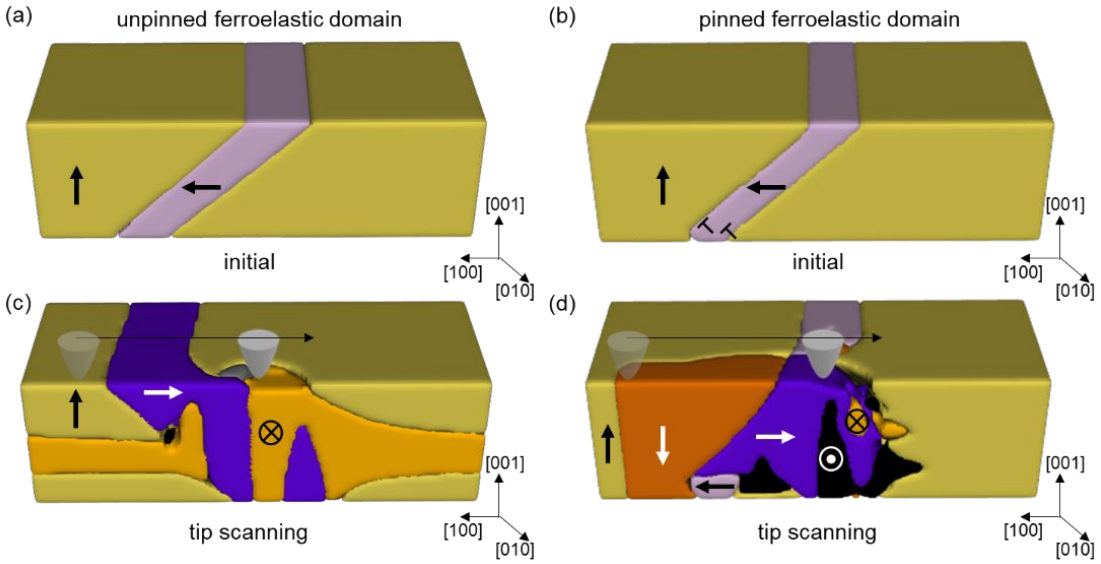

Figure S6 Simulated domain structure evolution under a scanning tip for the models with (a,c) unpinned and (b,d) pinned ferroelastic domains. (a,b) The initial domain structure before applying tip pressure. (c,d) The domain structure under pressure after the tip scans across the pre-existing ferroelastic domains. The arrows denote the polarization directions. Note that the misfit strain states are different in (a,c) and (b,d) in order to stabilize the initial a_1^+ domain.

In Movie S3, we show that when there is not a preexisting ferroelastic domain, tip pressure scan can induce ferroelastic domains around the contact region, which move toward the direction of the tip motion. However, these induced ferroelastic domain are unstable after unloading, because of the large compressive misfit strain in the system ($\varepsilon_{xx} = \varepsilon_{yy} =$ -1.0%). To make a comparative study, we reduce the clamping misfit strain ($\varepsilon_{xx} = \varepsilon_{yy} = -0.2\%$) while keeping all other conditions the same. Then, we perform the simulation for the case of an unpinned ferroelastic domain, and compare its results with the case of a ferroelastic domain pinned by a pair of interfacial dislocations as presented in the main text.

As shown in Fig. S6a,c, there is no 180-degree domain switching observed in the unpinned ferroelastic domain model. Instead, the tip pressure induces a large a_2^- domain (orange color) running throughout the [100] direction together with an a_1^- domain (purple color). These two ferroelastic domain forms a cross pattern if looking from the out-of-plane direction. They move along with the tip motion, and after unloading relax to a crossing domain structure that is typically seen in low biaxially-strained $PbTiO_3$ epitaxial films. Likewise, when the tip scans in a reversed direction, another combination of the crossing ferroelastic domains (a_1^+ and a_2^+ domains) can form under the pressure, move with the tip, and stabilize after unloading (not shown here).

■ SUPPLEMENTARY MOVIES

Movie S1 Continuous PFM imaging under a high loading force of 1500 nN using a diamond tip

Movie S2 Simulated domain evolution during tip scanning across an embedded a_1^+ domain

Movie S3 Simulated domain evolution during tip scanning in a single c^+ domain